

Birefringent all-solid hybrid microstructured fiber

Ryuichiro Goto¹, Stuart D. Jackson¹, Simon Fleming¹,
Boris T. Kuhlmeiy², Benjamin J. Eggleton², and Kuniharu Himeno³

¹*Optical Fibre Technology Centre and School of Physics, University of Sydney,
206 National Innovation Centre, Australian Technology Park, Eveleigh, NSW 1430, Australia*

²*Centre for Ultrahigh-bandwidth Devices for Optical Systems (CUDOS), School of Physics,
University of Sydney, NSW 2006, Australia*

³*Optics and Electronics Laboratory, Fujikura Ltd., Sakura, Chiba 285-8550, Japan*

ryugoto@physics.usyd.edu.au

Abstract: We report the characterization of a birefringent all-solid hybrid microstructured fiber, in which the core-modes are guided by both the photonic bandgap (PBG) effect and total internal reflection (TIR). Due to the twofold symmetry, modal birefringence of 1.5×10^{-4} and group birefringence of 2.1×10^{-4} were measured at $1.31 \mu\text{m}$, which is in the middle of the second bandgap. The band structure was calculated to be different from conventional 2-D PBG fibers due to the 1-D arrangement of high-index regions. The bend loss has a strong directional dependence due to the coexistence of the two guiding mechanisms. The fiber has two important properties pertinent to PBG fibers; spectral filtering, and chromatic dispersion specific to PBG fibers. The number of high-index regions, which trap pump power (by index guiding) when the fiber is used in cladding-pumped fiber lasers, is greatly reduced so that this fiber should enable efficient cladding pumping. This structure is suitable for linearly-polarized, cladding-pumped fiber lasers utilizing the properties of PBG fibers.

© 2008 Optical Society of America

OCIS codes: (060.2310) fiber optics; (060.2400) fiber properties.

References and links

1. F. Brechet, P. Roy, J. Marcou, and D. Pagnoux, "Single-mode propagation into depressed-core-index photonic-bandgap fibre designed for zero-dispersion propagation at short wavelengths," *Electron. Lett.* **36**, 514–515 (2000).
2. J. Riishede, J. Lægsgaard, J. Broeng, and A. Bjarklev, "All-silica photonic bandgap fibre with zero dispersion and a large mode area at 730 nm," *J. Opt. A* **6**, 667–670 (2004).
3. F. Luan, A. K. George, T. D. Hedley, G. J. Pearce, D. M. Bird, J. C. Knight, and P. St. J. Russell, "All-solid photonic bandgap fiber," *Opt. Lett.* **29**, 2369–2371 (2004).
4. A. Argyros, T. A. Birks, S. G. Leon-Saval, C. M. Cordeiro, F. Luan, and P. St. J. Russell, "Photonic bandgap with an index step of one percent," *Opt. Express* **13**, 309–314 (2005). URL <http://www.opticsexpress.org/abstract.cfm?URI=oe-13-1-309>.
5. P. Yeh, A. Yariv, and E. Marom, "Theory of Bragg fiber," *J. Opt. Soc. Am.* **68**, 1196–1199 (1978).
6. J. C. Knight, J. Broeng, T. A. Birks, and P. St. J. Russell, "Photonic Band Gap Guidance in Optical Fibers," *Science* **282**, 1476–1478 (1998).
7. T. A. Birks, P. J. Roberts, P. St. J. Russell, D. M. Atkin, and T. J. Shepherd, "Full 2-D photonic bandgaps in silica/air structures," *Electron. Lett.* **31**, 1941–1943 (1995).
8. J. Lægsgaard, "Gap formation and guided modes in photonic bandgap fibres with high-index rods," *J. Opt. A* **6**, 798–804 (2004).
9. T. P. White, R. C. McPhedran, C. Martijn de Sterke, N. M. Litchinitser, and B. J. Eggleton, "Resonance and scattering in microstructured optical fibers," *Opt. Lett.* **27**, 1977–1979 (2002).

10. N. M. Litchinitser, A. K. Abeeluck, C. Headley, and B. J. Eggleton, "Antiresonant reflecting photonic crystal optical waveguides," *Opt. Lett.* **27**, 1592–1594 (2002).
11. A. Wang, A. K. George, and J. C. Knight, "Three-level neodymium fiber laser incorporating photonic bandgap fiber," *Opt. Lett.* **31**, 1388–1390 (2006).
12. V. Pureur, L. Bigot, G. Bouwmans, Y. Quiquempois, M. Douay, and Y. Jaouen, "Ytterbium-doped solid core photonic bandgap fiber for laser operation around 980 nm," *Appl. Phys. Lett.* **92**, 061113 (2008).
13. A. Isomäki and O. G. Okhotnikov, "Femtosecond soliton mode-locked laser based on ytterbium-doped photonic bandgap fiber," *Opt. Express* **14**, 9238–9243 (2006). URL <http://www.opticsexpress.org/abstract.cfm?URI=oe-14-20-9238>.
14. G. Bouwmans, L. Bigot, Y. Quiquempois, F. Lopez, L. Provino, and M. Douay, "Fabrication and characterization of an all-solid 2D photonic bandgap fiber with a low-loss region (< 20 dB/km) around 1550 nm," *Opt. Express* **13**, 8452–8459 (2005). URL <http://www.opticsexpress.org/abstract.cfm?URI=oe-13-21-8452>.
15. S. Février, R. Jamier, J.-M. Blondy, S. L. Semjonov, M. E. Likhachev, M. M. Bubnov, E. M. Dianov, V. F. Khopin, M. Y. Salganskii, and A. N. Guryanov, "Low-loss singlemode large mode area all-silica photonic bandgap fiber," *Opt. Express* **14**, 562–569 (2006). URL <http://www.opticsexpress.org/abstract.cfm?URI=oe-14-2-562>.
16. Y. Barannikov, A. Oussov, F. Shcherbina, R. Yagodkin, V. Gapontsev, and N. Platonov, "250 W, single-mode, CW, linearly-polarized fibre source in Yb wavelength range," in *Proceedings of Conference on Lasers and Electro-Optics (Optical Society of America, 2004)*, paper CMS3 (2004).
17. J. K. Lyngsø, B. J. Mangan, and P. J. Roberts, "Polarization maintaining hybrid TIR / bandgap all-solid photonic crystal fiber," in *Proceedings of Conference on Lasers and Electro-Optics, and Conference on Quantum Electronics and Laser Science (Optical Society of America, 2008)*, paper CThV1 (2008).
18. R. Goto, K. Takenaga, K. Okada, M. Kashiwagi, T. Kitabayashi, S. Tanigawa, K. Shima, S. Matsuo, and K. Himeno, "Cladding-Pumped Yb-Doped Solid Photonic Bandgap Fiber for ASE Suppression in Shorter Wavelength Region," in *Proceedings of Conference on Optical Fiber communication/National Fiber Optic Engineers Conference (Optical Society of America, 2008)*, paper OTuJ5 (2008).
19. A. Cerqueira, S. Jr., F. Luan, C. M. B. Cordeiro, A. K. George, and J. C. Knight, "Hybrid photonic crystal fiber," *Opt. Express* **14**, 926–931 (2006). URL <http://www.opticsexpress.org/abstract.cfm?URI=oe-14-2-926>.
20. S. Johnson and J. Joannopoulos, "Block-iterative frequency-domain methods for Maxwell's equations in a planewave basis," *Opt. Express* **8**, 173–190 (2001). URL <http://www.opticsexpress.org/abstract.cfm?URI=oe-8-3-173>.
21. A. Argyros, T. A. Birks, S. G. Leon-Saval, C. M. B. Cordeiro, and P. S. J. Russell, "Guidance properties of low-contrast photonic bandgap fibres," *Opt. Express* **13**, 2503–2511 (2005). URL <http://www.opticsexpress.org/abstract.cfm?URI=oe-13-7-2503>.
22. T. A. Birks, F. Luan, G. J. Pearce, A. Wang, J. C. Knight, and D. M. Bird, "Bend loss in all-solid bandgap fibres," *Opt. Express* **14**, 5688–5698 (2006). URL <http://www.opticsexpress.org/abstract.cfm?URI=oe-14-12-5688>.
23. L. Xiao, W. Jin, and M. S. Demokan, "Photonic crystal fibers confining light by both index-guiding and bandgap-guiding: hybrid PCFs," *Opt. Express* **15**, 15,637–15,647 (2007). URL <http://www.opticsexpress.org/abstract.cfm?URI=oe-15-24-15637>.
24. T. Hosaka, K. Okamoto, Y. Sasaki, and T. Edauro, "Single mode fibres with asymmetrical refractive index pits on both sides of core," *Electron. Lett.* **17**, 191–193 (1981).
25. N. A. Issa and L. Poladian, "Vector wave expansion method for leaky modes of microstructured optical fibers," *J. Lightwave Technol.* **21**, 1005–1012 (2003). (Note that, in our paper, due to superior performance in most applications, a finite difference scheme is used in the radial direction instead of the basis function expansion described in the reference.)
26. X. Chen, M.-J. Li, N. Venkataraman, M. T. Gallagher, W. A. Wood, A. M. Crowley, J. P. Carberry, L. A. Zenteno, and K. W. Koch, "Highly birefringent hollow-core photonic bandgap fiber," *Opt. Express* **12**, 3888–3893 (2004). URL <http://www.opticsexpress.org/abstract.cfm?URI=oe-12-16-3888>.
27. W. J. Bock and W. Urbanczyk, "Measurement of polarization mode dispersion and modal birefringence in highly birefringent fibers by means of electronically scanned shearing-type interferometry," *Appl. Opt.* **32**, 5841–5848 (1993).
28. M. S. Alam, K. Saitoh, and M. Koshiba, "High group birefringence in air-core photonic bandgap fibers," *Opt. Lett.* **30**, 824–826 (2005).
29. J. Noda, K. Okamoto, and Y. Sasaki, "Polarization-maintaining fibers and their applications," *J. Lightwave Technol.* **4**, 1071–1089 (1983).
30. H.-T. Shang, "Chromatic dispersion measurement by white-light interferometry on metre-length single-mode optical fibres," *Electron. Lett.* **17**, 603–605 (1981).

1. Introduction

All-solid photonic bandgap (PBG) fibers [1–4] are one configuration of PBG fibers [5, 6] in which a low-index glass core is surrounded by a microstructured cladding, which typically

comprises isolated high-index glass regions embedded in a low-index glass background. The core-modes are guided not by total internal reflection (TIR) but by coherent multiple scattering from the microstructured cladding, and the guidance mechanism is explained by the PBG effect [7,8] or, more generally, by anti-resonant reflection [9,10]. A particularly interesting aspect of all-solid PBG fibers is that their core can be doped with rare-earth ions to make fiber lasers. Such fiber lasers then benefit from the properties of all-solid PBG fibers, such as spectral filtering [11,12], chromatic dispersion adjustable by design [1,2,13], and the potential to achieve large mode area [2,14,15].

Many applications of all-solid PBG fibers in fiber lasers require birefringence and the capacity for efficient cladding pumping. For example, when a high power fiber laser is used for frequency doubling, linearly polarized output from a fiber laser is required, so that the laser cavity preferably consists of cladding-pumped birefringent fibers and a polarizer [16]. To obtain high cladding pumping efficiency in all-solid PBG fibers, it is necessary to minimize the amount of pump power which is trapped (by index guiding) in the high-index regions, and hence not absorbed by the rare-earth doped core. It has been reported that birefringence in an all-solid PBG fiber can be realized by incorporating stress elements in a 2-D structure [17], however the reported structure has many high-index regions and therefore may suffer low cladding pumping efficiency.

With the aim of improving the cladding pumping efficiency of all-solid PBG fibers, we have previously reported a cladding-pumped, ytterbium-doped, all-solid hybrid microstructured fiber [18]. The fiber is based on a recently reported new form of microstructured fiber, in which the guidance mechanism is based on both the PBG effect and TIR [19]. The number of high-index regions is reduced more than ten times (from 126 to 12) compared to comparable 2-D structures, therefore high cladding pumping efficiency is expected. As a result of the twofold rotational symmetry of the fiber, birefringence is also expected.

In this paper, we report the characterization of an all-solid hybrid microstructured fiber having the same structure as previously reported [18] but having no ytterbium doping in the core. We measured modal birefringence of 1.5×10^{-4} and group birefringence of 2.1×10^{-4} at $1.31 \mu\text{m}$, which are due to the twofold symmetry. The contribution of stress and form birefringence to the modal birefringence is discussed. The measured group birefringence showed large wavelength dependency near the edges of the second bandgap. We calculated the band structure of the 1-D arrangement of high-index regions and found it to differ noticeably from conventional 2-D PBG fibers. The bend loss was measured to show a strong directional dependence due to the coexistence of the two guiding mechanisms. The fiber has two important properties of PBG fibers; spectral filtering, and chromatic dispersion specific to PBG fibers. This structure is suitable for linearly-polarized, cladding-pumped fiber lasers utilizing the properties of PBG fibers.

2. Fiber structure

The cross section of the fiber is schematically shown in Fig. 1(a). In the silica cladding (shown in light gray), the Ge-doped high-index regions (shown in white) with pure silica jackets (shown in light gray) are positioned periodically in the x-direction with pitch Λ . The diameters of the high-index regions and pure silica jackets are d_{high} and d_{si} . The remainder of the cross section comprises fluoride(F)-doped low-index uniform glass (shown in dark gray). The core is formed by replacing one high-index region with pure silica and the core diameter is d_{core} . Figure 1(b) shows the refractive index profiles along with the x- and y-axis of the fiber cross section. In the x-direction, the core is surrounded by the high-index regions and the guidance mechanism is based on the PBG effect. Along the y-axis, the core is surrounded by the low-index cladding and the guidance mechanism is based on TIR. The outer pure silica cladding surrounding the

low-index cladding is far from the core and the leakage loss through the low-index cladding is negligibly small.

The cross section of the fabricated hybrid microstructured fiber is shown in Fig. 2. The stack and draw method was used for fiber fabrication. First, a Ge-doped silica preform with pure silica cladding and a uniformly F-doped silica preform were both drawn into rods. These rods were then hexagonally stacked in a pure silica tube and drawn to a fiber. The pitch of the high-index regions, Λ , is $8.0 \mu\text{m}$. According to the measurement of the Ge-doped silica preform before being drawn into rods, Δn_{high} is about 2.8% and d_{high}/Λ is ~ 0.5 . The relative refractive index profile of the high-index regions is approximated by $\Delta n(r) = \Delta n_{high}[1 - (r/R)^{4.25}]$, where r is the distance from the center of the high-index region and $R = d_{high}/2$. The relative refractive index difference of the low-index cladding Δn_{low} is -0.35%. The fiber diameter is $148 \mu\text{m}$.

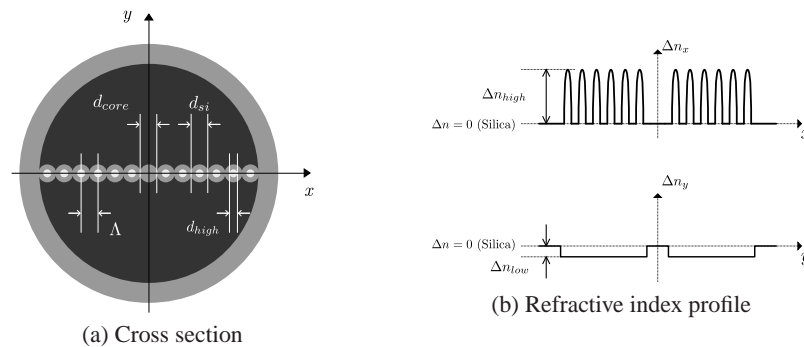


Fig. 1. Schematic cross section and refractive index profile of all-solid hybrid microstructured fiber.

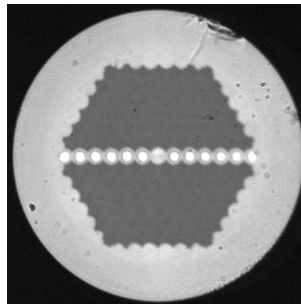


Fig. 2. Cross section of the hybrid microstructured fiber.

3. Fiber characterization

3.1. Transmission

First, we measured the transmission spectrum of the fiber with different bend radii. The measurements were taken using a supercontinuum (SC) source and an optical spectrum analyzer (OSA). The fiber length was two meters and the input and output ends were fusion spliced to a step index fiber ($\lambda_{cutoff} \sim 0.95 \mu\text{m}$) to measure core-modes. The fiber was coiled to three different radii; 160, 50, and 25 mm. For these measurements, no attention was paid to the bend direction of the fiber relative to the direction of the high-index regions. The transmission spectra of the fiber for the three different radii are shown in Fig. 3. The spectra are normalized with

regard to the spectrum of the SC source. The second, third, and fourth bandgaps were observed in the wavelength regions centered at 1400, 900, and 700 nm. Additional but weaker transmission windows were observed between these bandgaps. These weak transmission windows are not observed in 2-D PBG fibers. They are sensitive to fiber bending, and almost disappear as the coiling radius is reduced.

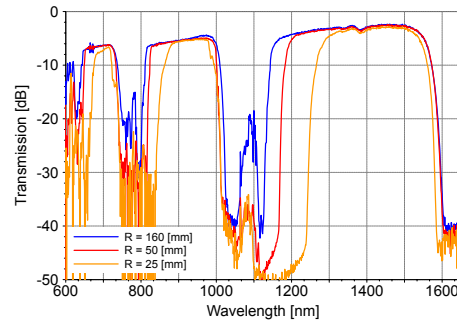


Fig. 3. Transmission spectra of the hybrid microstructured fiber.

To analyze the origin of these weak transmission windows observed in Fig. 3, we calculated the band structures of the hybrid microstructured fiber and a conventional 2-D PBG fiber having the same high-index region. The plane wave expansion method [20] was used for the calculation. Material dispersion was neglected and the refractive index of pure silica was fixed to 1.45 for simplicity. To resemble the real structure, we assumed that d_{core} and d_{si} were both $8.8 \mu\text{m}$ in our calculations and hence we assumed the core and circular microstructural elements are overlapping by $0.8 \mu\text{m}$. Λ , d_{high} , $\Delta n(r)$, and Δn_{low} are the same as in the previous section.

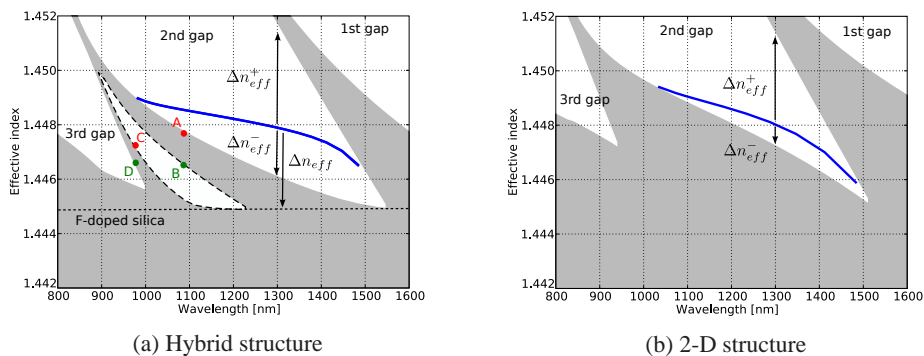


Fig. 4. Calculated band structure and fundamental core-mode of the hybrid and 2-D structure. The core-mode is shown only in the second bandgap for simplicity. 7×7 supercell is used for the calculation.

Figures 4(a) and (b) show the band structures of the hybrid and 2-D PBG fibers. In Fig. 4(a), $n_{eff} \sim 1.445$ corresponds to the refractive index of the F-doped low-index cladding and no bandgap exists below this line. Shown as a solid line is the fundamental core-mode in the second bandgap. The calculated transmission range is in reasonable agreement with the experiments, the difference may be attributed to the changes in the refractive index profile and shape when the preform was drawn to the fiber. When compared with the 2-D PBG structure [see Fig. 4(b)], it is seen that the hybrid structure has an additional bandgap [region surrounded by the dotted

line in Fig. 4(a)] between the second and third bandgaps. Indeed, poorly confined core-modes were found within the additional bandgap in our calculation and this explains the weak transmission window observed around 1100 nm in Fig. 3. The formation of this additional bandgap is explained by considering how bands are formed by high-index regions. Bands formed from high-index regions are determined by (1) the modes of each high-index region and (2) how high-index region modes couple and form a set of supermodes [8]. According to this model, the set of supermodes between the second and third bandgaps is formed by the LP21 and LP02 modes of each high-index region. In the hybrid structure, high-index regions only exist in the x-direction, limiting the formation of broadband supermodes, and an additional bandgap appears between the LP21 and LP02 modes of the high-index regions. Figures 5(a) and (b) show two typical intensity profiles of the supermodes between the second and additional bandgaps; Figs. 6(a) and (b) show the intensity profiles of the supermodes between the third and additional bandgaps. In the figures, the border of the pure silica jackets and the low-index F-doped cladding is shown as solid lines. As the figures clearly show, the band of supermodes between the second and additional bandgaps is formed by the LP02-based supermodes, and that between the third and additional bandgaps is formed by the LP21-based supermodes. These additional bandgaps may be eliminated by a modified design. In our calculations, as we increased d_{high}/Λ , the high-index regions became more coupled and the additional bandgap disappeared.

It should be noted that the LP11 core-mode was found in the additional bandgap in our calculation, therefore the fiber may be multi-moded in the shorter wavelength region of the second bandgap. The results presented hereafter all relate to the fundamental mode because, in the experiments, a launch fiber was spliced to the hybrid fiber to excite only the core-modes of the fiber and the launch fiber is single-mode within the wavelength range of the measurements; the fundamental core-mode of the hybrid fiber was therefore selectively excited.



(a) $\lambda = 1.09 \mu\text{m}$, $n_{eff}=1.4476$ [A in Fig. 4 (a)] (b) $\lambda = 1.09 \mu\text{m}$, $n_{eff}=1.4464$ [B in Fig. 4 (a)]

Fig. 5. Typical intensity profiles of the LP02-based supermodes between the second and additional bandgaps of the hybrid structure.



(a) $\lambda = 0.98 \mu\text{m}$, $n_{eff}=1.4473$ [C in Fig. 4 (a)] (b) $\lambda = 0.98 \mu\text{m}$, $n_{eff}=1.4466$ [D in Fig. 4 (a)]

Fig. 6. Typical intensity profiles of the LP21-based supermodes between the third and additional bandgaps of the hybrid structure.

Figure 7 shows the loss spectrum of the fiber in the second bandgap. A minimum loss of 8 dB/km was measured at 1300 nm using a 66 m-length fiber, which was spooled on a 160 mm-diameter bobbin. We believe that the measured loss is sufficiently low for most fiber laser applications. The loss increase around 1240 and 1380 nm originates from OH ions, as no special care was taken to reduce OH content in the fiber during fiber fabrication.

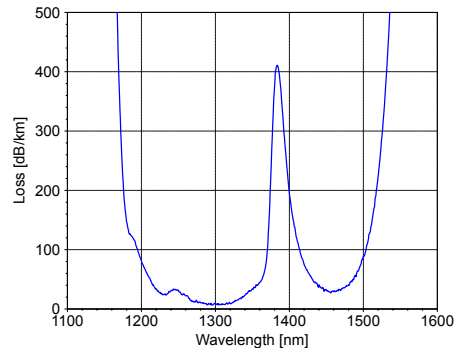


Fig. 7. Loss spectrum of the hybrid microstructured fiber.

3.2. Bend loss

The fiber should have two bend loss mechanisms, relating to each of the guidance mechanisms. To confirm this, we measured the directional dependency of bend loss of this fiber. The experimental setup is shown in Fig. 8. A half-turn bend was applied to a 1 m-length fiber using a mandrel (Radius = 12.5 mm) and the bend loss was measured as a function of the bend angle θ . The results are shown in Fig. 9. When $\theta = 0^\circ$, almost no bend loss was observed, because the dominant mechanism of bend loss is that of fibers guided by TIR and TIR is still maintained. On the other hand, when $\theta = 90^\circ$, significant bend loss appeared at both short and long wavelength edges of the transmission range, because the dominant mechanism of bend loss is now that of all-solid PBG fibers and the bend changed the band structure of the fiber [21]. This property may practically be beneficial to reduce bend loss of all-solid PBG fibers, if the fiber (or its coating) has a non-circular shape which forces the fiber to be bent in the $\theta = 0^\circ$ direction.

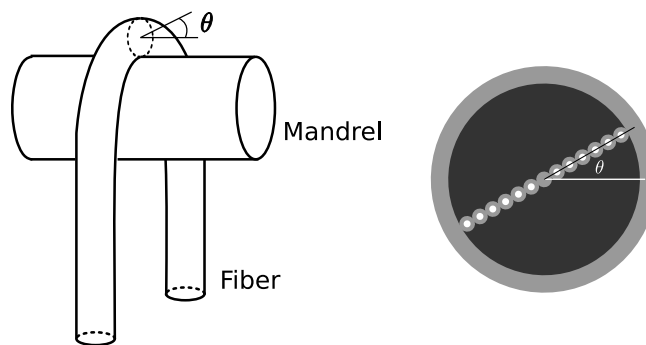


Fig. 8. Setup for angle dependency measurement of bend loss.

We next qualitatively compare the bend loss of the hybrid fiber with a comparable 2-D PBG fiber by comparing the band structures. By comparing Fig. 4(a) and (b), it is seen that the hybrid

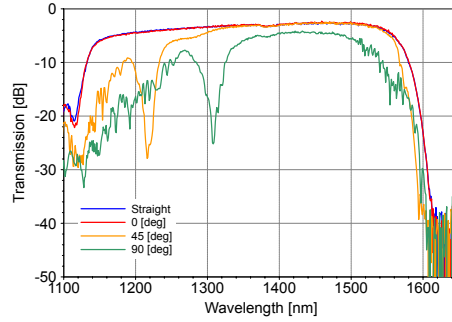


Fig. 9. Measurements of angle dependency of bend loss.

structure has deeper bandgaps, i.e., has large bandgaps in the direction of the effective index. The deeper bandgaps are realized by reduced mode coupling between the high-index regions and give the fiber reduced bend loss [22]. To understand the bend loss sensitivity, we consider two cases, $\theta = 0^\circ$ and 90° . When $\theta = 0^\circ$, the origin of the bend loss is similar to fibers guided by TIR, thus the refractive index difference between the core-modes to the low-index cladding [shown in Fig. 4(a) as Δn_{eff}] is a good measure of bend loss sensitivity. When $\theta = 90^\circ$, the origin of the bend loss is similar to PBG fibers, thus the refractive index differences between the core-modes to the nearest supermodes (shown in Fig. 4 as Δn_{eff}^+ and Δn_{eff}^-) is a good measure of bend loss sensitivity [22]. In both cases, these differences are larger for the hybrid microstructured fiber compared to the 2-D PBG fiber. This suggests that this hybrid fiber should show reduced bend sensitivity compared to the 2-D PBG fiber regardless of the bend angle θ .

3.3. Birefringence

The hybrid microstructured fiber has only twofold symmetry, so that the fiber has both form birefringence [23] and stress birefringence [17]. The stress birefringence of the hybrid microstructured fiber arises from the one-dimensionally arranged highly Ge-doped regions, which have a higher thermal expansion coefficient compared to pure silica.

Modal birefringence is generally the most important parameter for a polarization maintaining fiber (PMF) since it is a direct measure of the ability to maintain linear polarization. When both stress and form birefringence contribute to the birefringence, the total modal birefringence (B_m) is the sum of the modal birefringence due to stress birefringence (B_{ms}) and form birefringence (B_{mf}), i.e.,

$$B_m(\lambda) = B_{ms}(\lambda) + B_{mf}(\lambda). \quad (1)$$

The B_m of the fiber was measured by a cut-back method [24]. Linearly polarized light (polarized at 45° relative to the x-axis of the fiber) was launched into the core of the fiber. A single-mode launch fiber was spliced to the input end of the fiber to excite the fundamental core-mode. We used a short launch fiber (less than 5cm) and kept it straight so that the change of the polarization state in the launch fiber is minimized. A rotatable polarizer was positioned at the output of the fiber, and the degree of linear polarization (DOLP) at the output was determined by finding the angles where the maximum and minimum output are obtained. DOLP is defined by

$$DOLP = \frac{I_{max} - I_{min}}{I_{max} + I_{min}} \quad (2)$$

where I_{max} and I_{min} in Eq. (2) are the maximum and minimum output power through the polarizer. The fiber length was initially 1 m and was shortened by 500 μm or 1 mm in each polarization measurement, and the DOLP was measured as a function of the removed fiber length. For this measurement, we used a laser diode operating at 1.31 μm , which is nearly at the center of the second bandgap. Figure 10 shows the measured DOLP as a function of the removed fiber length. A DOLP oscillation with a period of ~ 4.5 mm is observed, which indicates the beatlength is 9 mm. The beatlength corresponds to modal birefringence of 1.5×10^{-4} at 1.31 μm . The measured modal birefringence is comparable to that of conventional PMFs so this fiber can be used as a PMF.

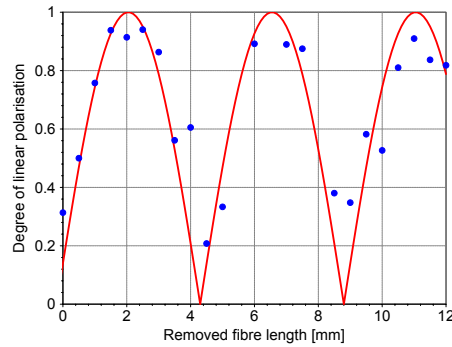


Fig. 10. Measured DOLP as a function of removed fiber length.

To analyze the origin of the modal birefringence, we also calculated the B_{mf} using the ABC-FDM method [25]. The calculated B_{mf} , however, was of the order of 10^{-6} in the middle of the bandgap and the difference between this value and the measurement is more than an order of magnitude. We believe that the measured mode birefringence is primarily related to the B_{ms} arising from the high-index regions at this wavelength.

We measured the group birefringence by the fixed analyzer method and the Jones matrix eigenanalysis (JME). For the fixed analyzer method, broadband light from a SC source was launched into the fiber through a polarizer and the output from the fiber was detected by an OSA after another polarizer. We used a 2 m-length fiber. Two single-mode fibers with negligible birefringence were spliced to both ends of the hybrid microstructured fiber to selectively measure the fundamental core-mode. Figure 11(a) shows the measured spectrum. The measured spectrum was not normalized and the dip around 1400 nm is due to the output spectrum of the SC source. Figure 11(a) shows the measured power as a function of the wavelength; the oscillation is due to the birefringence of the fiber. This oscillation is clearly shown in the detailed spectra in Figs. 11(b) and (c). The group birefringence $B_g(\lambda)$ is given by

$$B_g(\lambda) = \frac{\lambda^2}{L\Delta\lambda} \quad (3)$$

where L is the length of the fiber, λ is the wavelength, and $\Delta\lambda$ is the wavelength difference between two peaks of the oscillation [26]. Interestingly, the period of the oscillation becomes very large around 1160 nm and 1540 nm. This implies that the group birefringence becomes zero and changes sign around these two wavelengths. Taking this into account, we calculated the group birefringence using Eq. (3). The result is shown in Fig. 11(d) as a blue curve. The group birefringence changes sign quite smoothly at these two wavelengths, supporting the assumption that the group birefringence becomes zero. The two red curves shown in Fig. 11(d) are the measured group birefringence by the JME using a 2 m-length fiber. The wavelength

range was limited by the availability of tunable light sources. The sign of the measured group birefringence was changed accordingly, based on our assumption that the group birefringence becomes zero and changes sign around 1540 nm. These two results are in good agreement. It should be noted that the sign of the group birefringence is not determined by these experimental methods, thus the sign is arbitrary in Fig. 11(d).

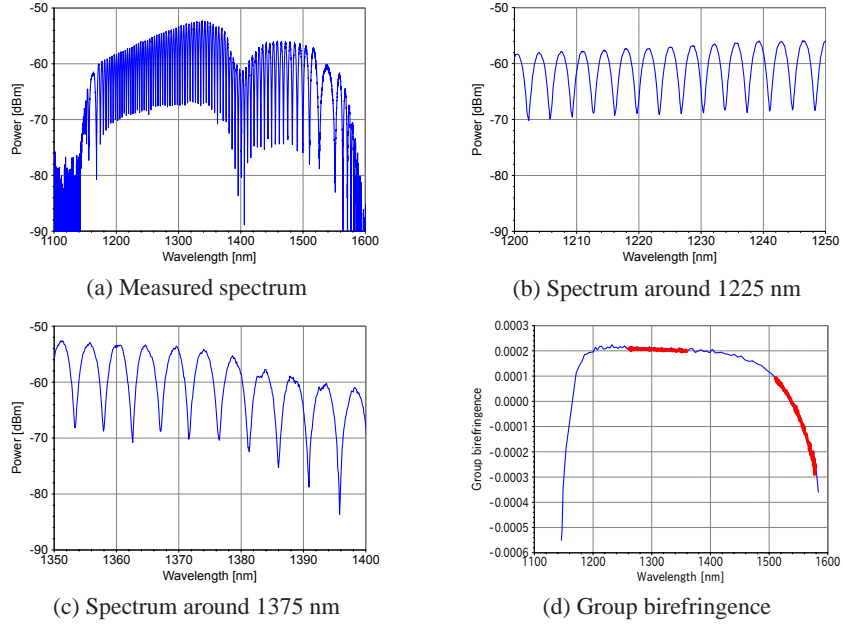


Fig. 11. Measurements of the group birefringence.

The difference between the measured modal and group birefringence in the middle of the bandgap is relatively large. In addition, the measured group birefringence changes sign near the edges of the bandgap. These results are quite different from conventional PMFs such as PANDA or Bow-Tie fibers, in which the difference between the two birefringence values is very small [27], and the group birefringence has the same sign within the entire operating wavelength range. To analyze these two unusual results, consider the definition of group birefringence (B_g) which is given by,

$$B_g(\lambda) = B_m(\lambda) - \lambda \frac{dB_m}{d\lambda}. \quad (4)$$

Equation (4) shows that B_m and B_g can differ significantly when $dB_m/d\lambda$ is large, i.e., when B_m is highly wavelength dependent. The measured difference between B_m and B_g is therefore attributed to the relatively large wavelength dependence of B_m in the middle of the bandgap. The large wavelength dependency of B_m could be both due to stress and form birefringence. By substituting Eq. (1) into Eq. (4), we obtain

$$B_g(\lambda) = B_{gs}(\lambda) + B_{gf}(\lambda) \quad (5)$$

where

$$B_{gs}(\lambda) = B_{ms}(\lambda) - \lambda \frac{dB_{ms}}{d\lambda} \quad (6)$$

$$B_{gf}(\lambda) = B_{mf}(\lambda) - \lambda \frac{dB_{mf}}{d\lambda}. \quad (7)$$

In Eqs. (5)-(7), B_{gs} and B_{gf} stand for group birefringence due to stress and form birefringence, respectively. It has been reported that B_{gf} of a PBG fiber can be an order of magnitude larger than the B_{mf} [28], because B_{mf} is highly wavelength dependent and the second term on the right-hand side of Eq. (7) becomes large. In our calculation using the ABC-FDM method, in the middle of the bandgap, the second term on the right-hand side of Eq. (7) was smaller than 10^{-5} , however, the value was sensitive to parameters of the calculation and can exceed 10^{-5} by small changes in the parameters; the second term on the right-hand side of Eq. (7) may partially explain the difference between the measured B_m and B_g . In addition, in our hybrid fiber, the B_{ms} can be highly wavelength dependent and the second term on the right-hand side of Eq. (6) may contribute to the difference between the measured B_m and B_g , since stress birefringence is the convolution of the modal field and stress field [29] and the modal field should be more wavelength dependent than conventional fibers guided by TIR only, given that the guidance mechanism in the x-direction is based on coherent multiple scattering.

With regard to the change in sign of B_g near the edges of the bandgap, Ref. [28] shows that the wavelength dependence of B_{mf} becomes even larger near the edges of a bandgap. Our calculation using the ABC-FDM method also showed a similar trend. The wavelength dependence of B_{gs} should also become larger near the edges of a photonic bandgap, as the modal field becomes more wavelength dependent as the core-mode becomes leaky near the edges of a bandgap. The change in sign of B_g near the edges of the bandgap therefore may be explained by an even larger effect from the second term on the right-hand side of Eqs. (6) and (7).

3.4. Chromatic dispersion

The chromatic dispersion of the fiber was measured by an interferometric method [30] and the modulation phase-shift (MPS) method. We used a 27 cm-length fiber for the interferometric method. Two polarizers, which were aligned to the x-axis of the fiber, were used in the two arms of the interferometer. The measured relative group delay and chromatic dispersion are shown in Figs. 12(a) and (b). We aligned the polarizers to the y-axis and measured the chromatic dispersion, the difference was within the measurement accuracy. The measured result is shown in Fig. 12(b) as a red curve. The red curve was obtained by fitting the relative group delay to a 4th order polynomial. The fiber is highly dispersive and we were unable to fit the whole data using a single polynomial, therefore the data was divided into three sections and fitted using three different polynomials. Dots were obtained by differentiating the relative group delay. The two green curves in Fig. 12(b) are the measured chromatic dispersion by the MPS method using a 95 m-length fiber. The wavelength range was limited by the availability of tunable light sources and the input polarization was not aligned to the polarization axes of the fiber. These two results are in good agreement. Figure 12(b) shows that the chromatic dispersion is negative at the shorter edge of the bandgap, becomes zero in the bandgap, and is positive at the longer edge of the bandgap. This is a typical chromatic dispersion property of PBG fibers.

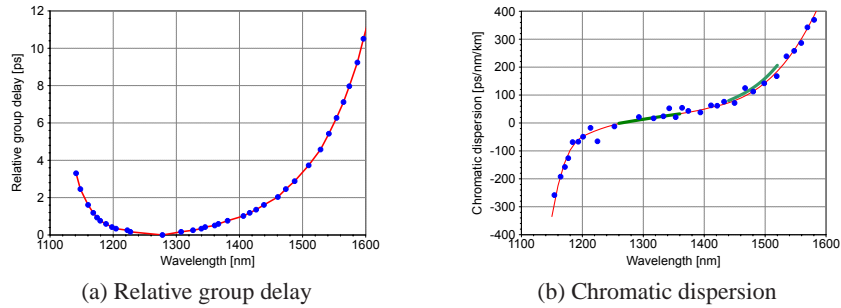


Fig. 12. Chromatic dispersion of the fiber.

4. Conclusions

We have reported a birefringent all-solid hybrid microstructured fiber. The twofold symmetry induces modal and group birefringence, which were measured to be 1.5×10^{-4} and 2.1×10^{-4} at $1.31 \mu\text{m}$. We suggest that stress birefringence is the dominant factor to the modal birefringence in the middle of the second bandgap, and the group birefringence may be affected by the large wavelength dependence of the modal birefringence. The band structure of the fiber was calculated to be different from conventional 2-D PBG fibers due to the 1-D arrangement of high-index regions, and the weak transmission windows characteristically measured in this hybrid fiber were explained by the difference of the band structure. Bend loss measurement (Radius = 12.5 mm) showed, that when the fiber is bent in the $\theta = 0^\circ$ direction, the bend loss is negligibly small because the band structure is unchanged and TIR is maintained, while when the fiber is bent in the $\theta = 90^\circ$ direction, the bend loss is significant because the band structure is altered by the bend. The number of high-index regions being greatly reduced compared with conventional 2-D PBG fibers, cladding pumping is expected to be much more efficient in this hybrid fiber, whilst maintaining two important properties of PBG fibers; spectral filtering, and chromatic dispersion specific to PBG fibers. This structure should thus be a promising candidate for realizing linearly-polarized, cladding-pumped fiber lasers utilizing the properties of PBG fibers.

Acknowledgments

The authors acknowledge the Optical Fiber Technology Group, Optics and Electronics Laboratory, Fujikura for supplying the fibers, and providing their results of the group birefringence and chromatic dispersion measurements by the JME and the MPS method. A. Docherty is acknowledged for providing the ABC-FDM code and support. A. Michie is acknowledged for useful discussions. The authors thank M. Large, M. van Eijkelenborg, A. Argyros, and S. G. Leon-Saval for access to the SC source. R. Goto acknowledges the Department of Education, Science and Training, Australia for financial support. This work was produced with the assistance of the Australian Research Council under the ARC Centre of Excellence program and the discovery project program (DP0665032). CUDOS is an ARC Centre of Excellence.